Large-Eddy Simulation of Flows Over Random Urban-Like Obstacles

Zheng-Tong Xie[1], Omduth Coceal[2] and Ian P Castro[1]

1 School of Engineering Sciences, University of Southampton, SO17 1BJ, UK
2 Department of Meteorology, University of Reading, P.O. Box 243, Reading RG6 6BB, U.K.

Abstract. Further to our previous Large-Eddy Simulation (LES) of flow over a staggered array of uniform cubes (Xie & Castro, 2006), a simulation of flow over random urban-like obstacles is presented. To gain a deeper insight into the effects of randomness in the obstacle topology, the current results, e.g. spatially averaged mean velocity, Reynolds stresses, turbulence kinetic energy (TKE) and dispersive stresses, are compared with our previous LES data and Direct Numerical Simulation (DNS) data (Coceal *et al.*, 2006) of flow over uniform cubes. Significantly different features in the turbulence statistics are observed within and immediately above the canopy, although there are some similarities in the spatially-averaged statistics. It is also found that the relatively high pressures on the tallest buildings generate contributions to the total surface drag which are far in excess of their proportionate frontal area within the array. Details of the turbulence characteristics (like the stress anisotropy) are compared with those in regular roughness arrays and attempts to find some generality in the turbulence statistics within the canopy region are discussed.

Keywords: Large-Eddy Simulation, Randomness, Urban Canopy, Generality of Turbulence Statistics

1. INTRODUCTION

Understanding the dominant physical mechanisms in flows over arrays of obstacles is directly beneficial to understanding of both building aerodynamics and urban meteorology. It is thus a vital ingredient in understanding pollutant dispersion processes within urban environments. Flow over regular arrays of cubes mounted on a wall has been studied by a number of researchers (Meinders & Hanjalić, 1999; Hanna *et al.*, 2002; Cheng & Castro, 2002; Stoesser *et al.*, 2003; Kanda *et al.*, 2004; Coceal *et al.*, 2006). These obstacles represent roughness elements - in the urban context, building blocks. However, the arrangement and sizes of buildings in a real urban area are random. As far as we are aware, except for the wind tunnel experiments of Cheng & Castro (2002) (hereafter, CC) the effects of randomness in the sizes or arrangement of blocks have thus far not been among the priorities in any previous work (either numerical simulation or wind tunnel experiment). In field studies (see Kastner-Kline & Rotach, 2004, for an example) such randomness is of course virtually guaranteed but its effects on the nature of the flow, as compared with flows over uniform, regular obstacle arrays, have seem not to have been explicitly investigated, apart from the recent study by Kanda (2006), who describes the use of LES to determine the effect of building height variations on total surface drag.

Before applying the results of simple wind tunnel models to flows over a full scale genuine array of buildings, numerous issues have to be addressed, e.g. possible Reynolds number dependence (discussed in our previous work, Xie & Castro, 2006). In the present

paper we address four questions. Firstly, to what extent do turbulence statistics within the canopy region and pressure on the surfaces of random blocks differ from those in an array of uniform blocks? There is already some experimental evidence, for example, that taller buildings can experience greater drag than would be anticipated on the basis solely of their frontal area (Hayden *et al.*, 2007). Secondly, to what extent is the turbulence within the roughness sublayer (RSL) and the canopy region (CR) for random arrays similar to that for uniform arrays? (The roughness sub-layer is defined here as that region above the roughness elements within which the flow remains spatially inhomogeneous in horizontal planes, with the canopy region the region below, encompassing all the roughness.) Thirdly, is it possible to identify a finite set of domains within the RSL and, particularly, the CR which each have different essential characteristics but could collectively be used to describe flows in *any* urban region by suitably combining them? For a uniform array of cubes Coceal *et al.* (2007a) have shown that this is feasible; whilst it might inherently seem more unlikely for general arrays, it would be practically very useful if it were possible. If it is not, is there any other alternative which would allow general characterisation of the flows within small urban regions? Fourthly, the details of flow within the RSL depend greatly on the arrangement and size of individual blocks. But how much detail is critical and cannot be ignored? This will also be intensively investigated in a related paper regarding coherent structures within the RSL of the random geometry flow discussed here.

Further to our previous LES and DNS of flows over a staggered array of uniform cubes, we have performed LES of the flow over a more urban-like array of obstacles. We took as a suitable array the one studied experimentally by CC, in which the size of a 'repeating unit' of the obstacles was 80mm x 80mm. For those experiments, each unit comprised an array of sixteen 10-mm-square elements having different heights chosen from an appropriate normal distribution. Of course, real urban geometries contain randomness not just in the building heights, but also in their shapes and in their placement with respect to each other. But the experiments were conceived as constituting a relatively simple initial probe of the effects of randomness. The impossibly large number of what one might call 'randomness variables' was thus limited essentially to just three - the variance in the building height, the number of buildings within a repeating unit and the relative positions of buildings of different heights within that unit. Because the earlier experiments used 10 mm cubes with 25% area coverage, the random array was chosen to use exactly the same plan arrangement and the same total volume of the blocks, with a 3 mm standard deviation in block height (and a mean height, h_m, of 10 mm). Other constraints leading to the choice of 16 blocks for the repeating unit are discussed by CC. For the present numerical study, four of these repeating units are included in the whole computing domain; this was thought sufficient for obtaining adequate statistics at least in the near-surface regions (the RSL and CR). Figure 1 shows one repeating unit of the surface used in the laboratory experiments of CC. The numerical results are compared where possible with available data from those experiments, which were somewhat limited compared with the present computations in that only data above the canopy were measured. The computations naturally provide much more complete data sets, throughout the entire domain, and allow an attack on the questions identified above. The governing equations and numerical details are outlined in

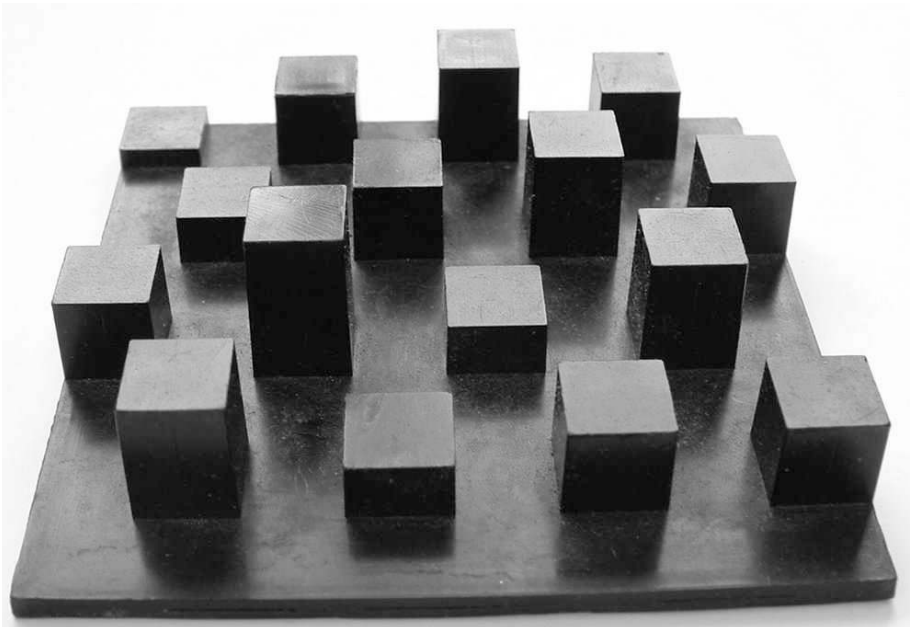

Figure 1. A view of one of the repeating units used in the experiments of Cheng & Castro (2002) and modelled numerically in the present work. The oncoming flow is from top to bottom.

the following section, results and discussion are presented in Section 3 and the final section provides some concluding remarks.

2. Governing Equations and Numerical Details

To ensure a largely self-contained paper, a brief description of the numerical methods is given here; more extensive details can be found in Xie & Castro (2006), hereafter denoted by XC.

The filtered continuity and Navier-Stokes equations are written as follows,

$$\begin{aligned} &\frac{\partial u_i}{\partial x_i} = 0 \\ &\frac{\partial u_i}{\partial t} + \frac{\partial u_i u_j}{\partial x_j} = -\frac{1}{\rho}\left(\frac{\partial p}{\partial x_i} + \delta_{i1}\frac{\partial \langle P \rangle}{\partial x_1}\right) + \frac{\partial}{\partial x_j}\left(\tau_{ij} + \nu\frac{\partial u_i}{\partial x_j}\right) . \end{aligned} \tag{1}$$

The dynamical quantities, u_i, p are resolved-scale (filtered) velocity and pressure respectively and τ_{ij} is the subgrid-scale (SGS) Reynolds stress. δ_{i1} is the Kronecker-delta and ν is the kinematic viscosity. $\partial\langle P\rangle/\partial x_1$ is the driving force, a constant streamwise pressure gradient. All the data presented in this paper were obtained using either FLUENT.v6 or STAR-CD4, run in LES mode. As discussed in XC, provided proper choices of mesh,

numerical (differencing) schemes and boundary conditions were used, essentially identical results were obtained with either code. The particular choices are identified below. For the sub-grid stresses the classical Smagorinsky SGS model was used in FLUENTv.6 with $C_s = 0.1$ and, in STAR-CD4, the very similar model discussed by Yoshizawa (1986) was used. In the near-wall region, the Lilly damping function was also applied; this reduces the filter width within the viscosity-affected region so that the energy-carrying eddy sizes scale appropriately. Also, for cases where the fine eddies in the vicinity of the wall are important, it is usually recommended that $\mathscr{N}_1^+$ is of order of unity (where $\mathscr{N}_1^+$ is the distance in wall units between the centroid of the first cell and the wall, assuming the $\mathscr{N}$ coordinate is normal to the wall). Note, however, that for a complex geometry, where separation and attachment processes occur, it is impossible to satisfy this criteria everywhere. We argue that, unlike the situation for smooth-wall flows, it is in fact not necessary, at least for obtaining overall surface drag and the turbulent motions at the scale of the roughness elements (buildings), which turn out to be dominant (see XC).

The local wall shear stress is then obtained from the laminar stress-strain relationships:

$$u^+ = \frac{u}{\hat{u}_\tau}, \quad \mathscr{N}^+ = \frac{\rho \hat{u}_\tau \mathscr{N}}{\mu}, \quad \mathscr{N}^+ = u^+ \,, \tag{2}$$

where $\rho \hat{u}_\tau^2$ is the local wall shear stress. However, if the near-wall mesh is not fine enough to resolve the viscous sublayer, for simplicity it is assumed that the centroid of the cell next to the wall falls within the logarithmic region of the boundary layer:

$$\frac{u}{\hat{u}_\tau} = \frac{1}{\kappa} \ln E \left(\frac{\rho \hat{u}_\tau \mathscr{N}}{\mu} \right), \tag{3}$$

where κ is the von Karman constant and E is an empirical constant - 7.77 to be consistent with Coles' values of the constants ($\kappa = 0.41, A = 5$) in the usual smooth-wall log-law formulation. The log-law is employed when $\mathscr{N}^+ > 11.2$. Again, note that for very rough-wall flows, even at very large Reynolds numbers, there are probably very few regions on the surface of the roughness elements where log-law conditions genuinely occur in practice. However, we have shown earlier that for this type of flow, where the individual elements are well resolved by the mesh, the precise surface condition is unimportant for capturing the element-scale flows and hence, for example, the surface drag (see XC). So it turns out that these various wall features of the computations (Lilly damping, log-law formulation, etc.) are not in fact important. Significant changes can be made to them without changing the nature of the overall flow significantly. In this sense, we argue that computations of very-rough-surface flows, resolving all roughness elements, is actually rather easier in some respects than computing smooth-wall flows with LES.

Crucially, the discretisation for all terms in Eq. (1) was second order accurate in both space and time. For time stepping, a second-order backward implicit scheme was used. For spatial differencing, we used either a deferred correction second order central scheme (for the hexahedral mesh, Fig.3a) or the second order monotone advection and reconstruction

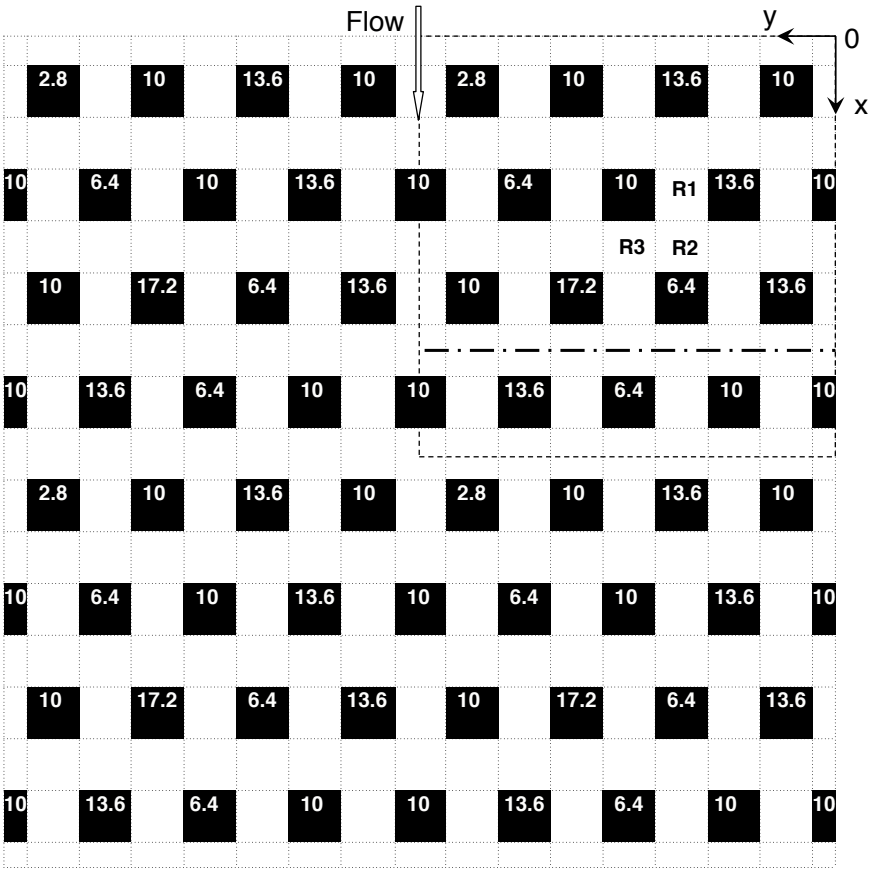

Figure 2. Plan view of computational domain. Numbers indicate the block height in mm, with each small square having an area of 10 x 10 mm^2. The large square highlighted by the dashed line indicates one of the four repeated units in the domain. The oncoming flow is from top to bottom. R1, R2, R3 respectively indicate what Coceal *et al.*(2007a) call a constricted region, a front-recirculation region and a building wake region.

scheme MARS (for the polyhedral mesh, Fig.3b). This latter scheme possesses the least sensitivity of solution accuracy to mesh structure (Moreau *et al.*, 2004). These multi-dimensional linear reconstruction schemes on face-based structures help to fulfill continuity and momentum conservation for cells with arbitrary topology (Choudhury *et al.*, 2004). The computational domain is illustrated in figure 2 and contained four repeating units (one of which is outlined by the dashed line), giving a domain size of $L_x \times L_y \times L_z = 16h_m \times 16h_m \times 10h_m$, where h_m is the mean height of the obstacles; the total number of obstacles was thus 64. Individual block heights are shown on the figure.

The constant pressure gradient in equation 1 was imposed on every cell as the driving force:

$$\frac{\partial P}{\partial x_1} = \frac{\rho u_\tau^2}{L_z}, \tag{4}$$

where u_τ is by definition the total wall friction velocity. The roughness Reynolds number, $Re_\tau = u_\tau h_m/\nu$, was 391, which is in the fully rough regime. The Reynolds number based on the maximum velocity (i.e. at $z = 10h_m$) and the mean height was approximately 4790. This is rather lower than the value used in the laboratory experiments (about 6700) but Reynolds number effects are relatively insignificant in these flows. This was demonstrated experimentally by Cheng & Castro (2002) in the context of cubic arrays, and was discussed by XC. As noted earlier, the turbulent motions at the roughness scale dominate, so that typical energy spectra contain significant inertial subranges above scales of order $h/10$ and the very thin boundary layers on the surfaces of the elements are unimportant. These facts mean that, unlike smooth-wall flows, Reynolds number effects are weak (and relatively course LES meshes can capture much of the inertial sub-range).

In the streamwise and lateral directions the flow was assumed periodic and at the top of the domain, stress free conditions were imposed. The computations thus actually represent fully-developed flow in a half-channel, which is both conceptually and practically rather easier than computing a boundary layer flow and is common in LES computations of atmospheric boundary layers (e.g. Moeng, 1984, Shaw & Schumann, 1992). Genuine boundary layer computations would preclude the use of periodic inlet/outlet conditions. Although there are techniques for inserting inlet turbulence (and we have ourselves developed a very efficient (filter-based) methodology – Xie & Castro, 2008), the emphasis in the present work is on the roughness sub-layer and canopy regions, so channel flow computations with a domain height not too dissimilar to the experimental boundary layer thickness are quite adequate (see also XC).

A three-level hexahedral mesh (2.3 million cells) with $16\times16\times16$ cells per $h_m\times h_m\times h_m$ in the near wall region (see Figure 3a) and a three-level polyhedral mesh (1.3 million cells) with $13 \times 13 \times 13$ cells per $h_m \times h_m \times h_m$ in the near wall region (see Figure 3b) were used in the FLUENTv.6 and STAR-CD4 computations, respectively. The time step was 0.002T ($T = h_m/u_\tau$). The initial duration of most of the runs was 150T, whereas the subsequent averaging duration for all the statistics was approximately $300T$. Coceal *et al.* (2006) found that for their array of uniform cubes, with a spanwise domain size of $8h_m$, the converging flow contained quite strong, large-scale structures having longitudinal vorticity. These rolls, typically having a spanwise wavelength of about $4h_m$, gave rise to significant dispersive stresses (i.e. stresses which arise from spatial inhomogeneities in the time-averaged fields) and adequate time-averaging was necessary to resolve statistics unequivocally (i.e. to reduce these dispersive stresses to zero above the near-wall region). They found that an averaging time of about $400T$ was necessary. For the present surface, there was little evidence of such rolls, partly no doubt because of the more random nature of the surface but also perhaps because the spanwise domain was limited to two repeating units (compared with four in Coceal *et al.*, 2006). So the $300T$ averaging time in the present case was quite sufficient for obtaining converged statistics.

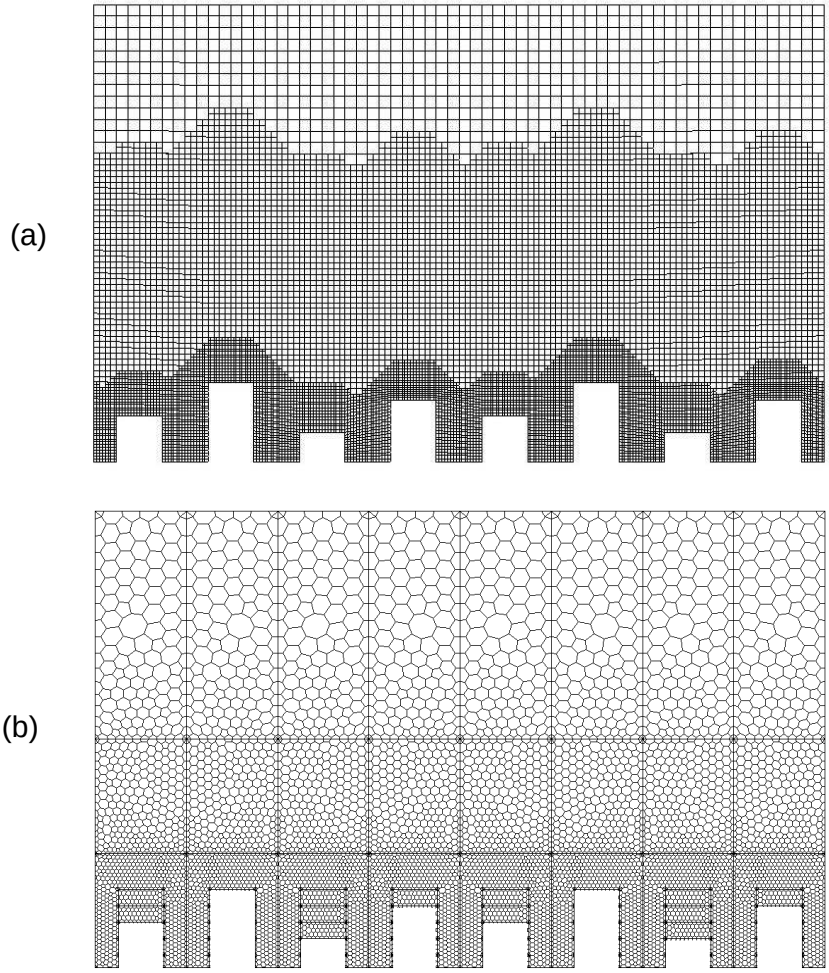

Figure 3. A vertical-transverse cut cross the tallest (17.2 mm) block. Hexahedral mesh (a) and polyhedral mesh (b).

3. Numerical results and data analysis

3.1. Validation

Essentially identical results were obtained using the hexahedral mesh (with Fluent6) and the polyhedral mesh (with Star-CD4). This suggests that the two meshes are both satisfactory, but it is known that polyhedral meshing is more flexible than the alternatives for complex geometries and it is also more accurate and less memory consuming than the widely used tetrahedral mesh (see, for example, Peric, 2004). Our earlier work (Xie

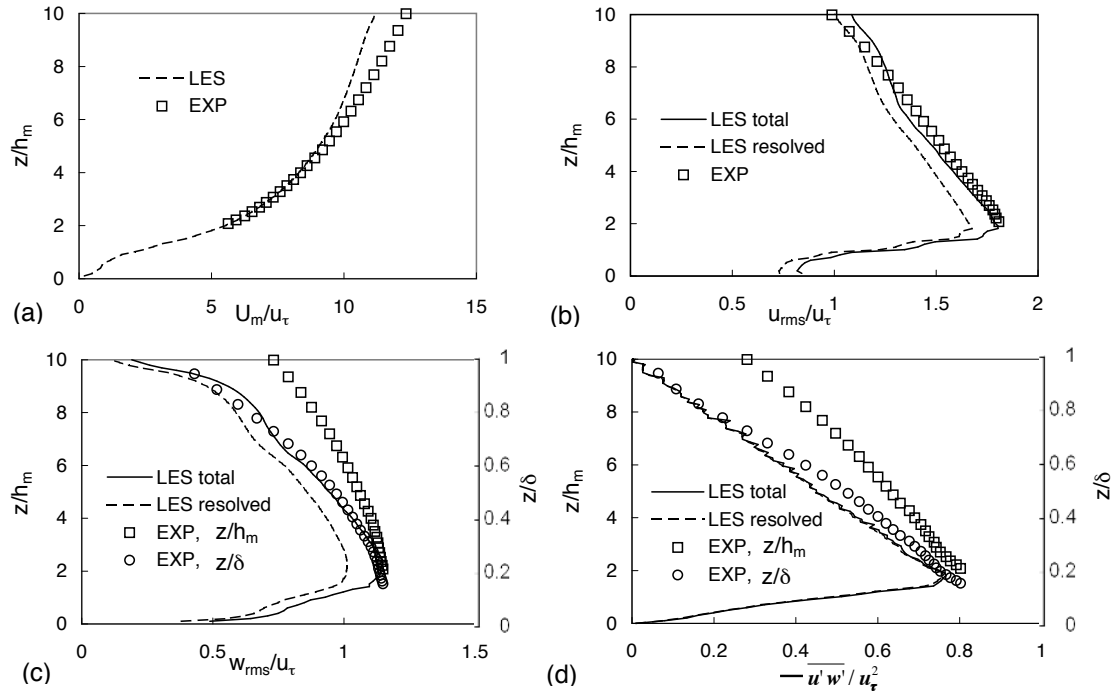

Figure 4. Spatially averaged mean velocity, velocity r.m.s. and Reynolds shear stress profiles. Open circles in (c) and (d) refer to the experimental data but have the ordinate, shown on the right, scaled by the boundary layer thickness.

& Castro, 2006), which addressed meshing issues in some detail, concluded that grid sizes around the obstacles should be no greater than about $0.06H$ for adequate LES computations of the canopy region (and thus the surface drag); the localised errors implied by relatively large changes in mesh spacing (e.g. around $z/h = 5$ in Fig.3a) were not found to prejudice overall solution accuracy.

Figure 4 plots the spatially averaged mean streamwise velocity, velocity r.m.s. and the Reynolds shear stress profiles. Note that the boundary layer thickness over the wind tunnel array was 137mm, while the depth of the computational domain is 100mm. This causes inevitable differences in the upper region of the domain for the quantities involving the vertical velocity fluctuations (i.e. w_{rms} and $\overline{u'w'}$). Normalising the height by the boundary layer thickness (or domain height) leads to much closer collapse, as shown in the figure. We emphasise here that although profiles over the entire domain height must clearly depend on the domain height – the latter is essentially a half-channel height (periodic conditions are used for inlet and outlet conditions and symmetry at the upper boundary, as discussed earlier) – the flow in the roughness sublayer is *not* strongly dependent on domain height. This was demonstrated by Coceal *et al.* (2006) and it allows sensible comparisons with the near-surface region of boundary layer flows over the same roughness, provided the boundary layer thickness is not too much smaller than the computational domain height.

Notice also that the sub-grid contributions to the r.m.s. velocities are not insignificant; in Fig.4b, for example, good agreement with experiment is obtained only once the sub-grid stress component is included. It is worth mentioning the rather subtle point that whilst it is not possible to calculate the sub-grid energy from the sub-grid stress tensor (whose trace is zero), one can approach the matter the other way around and *estimate* the sub-grid energy *posthoc* using the sub-grid model – which is supposed to represent the unresolved portion of the energy spectrum. This is what was done to deduce the additional contributions providing the (estimated) total stresses and energy in the Fig.4, but we emphasise that it is not strictly exact.

CC did not directly measure the total drag for the random surface. For the uniform surface they showed that the drag measured *via* a pressure tapped element (ignoring the viscous contribution) was some 30% higher than would be deduced using the measured Reynolds shear stress averaged through the RSL and the inertial sublayer. With the not unreasonable assumption that the same ratio holds for the random surface, the experimental values of the roughness length and zero plane displacement from the CC data are $z_o/h_m = 0.089$ and $d/h_m = 1.1$, respectively. Here, z_o and d have the usual meaning, as defined by the log law expressed as $\frac{U}{u_\tau} = \frac{1}{\kappa} ln(\frac{z-d}{z_o})$. The present LES data yield 0.095 and 1.2, respectively, which are satisfyingly close to the experimental values given the inherent uncertainties in the fitting process and the different outer flow conditions.

Figure 5 presents streamwise mean and *r.m.s.* velocity profiles behind row three (at $x/h_m = 6$, on the central line between rows three and four - see the chain-dotted line in fig.2). Each LES profile is an average of the available four profiles within the computational domain. The LES data are again in good agreement with the measurements except near the top of the domain (as noted earlier). Not surprisingly, the shape of the vertical profiles below about $z/h_m = 2$ depends on the height of the upstream obstacles in row three. So, for example, the mean flow profile at $y/h_m = 5$ (fig.5a) has a strong shear layer region around $z/h_m = 1.8$, because the block immediately upstream is the tallest block in the array (of height $1.73h_m$). One might then ask how much contribution the obstacles further upstream make to the turbulence profiles. Figure 6 shows a typical comparison between stations A and B. Station A is located $0.5h_m$ downstream of a 10mm block which is in the (axial) column containing the 17.2mm block, whereas station B is located $0.5h_m$ downstream of a 10mm block which is in the column containing the 2.8mm block (see fig. 7). Note that there are two clear peaks in the station A u_{rms} profile (fig. 6b) - a narrow one near $z = h_m$ marking the shear layer shed by the obstacle immediately upstream and a wider (larger) one near $z = 2h_m$, presumably arising from the shear layer shed at the top of the taller block further upstream. On the other hand, in the station B profiles the latter peak is relatively much more dominant, since the block further upstream is much lower. The experiment has few data within the canopy and thus the lower peak in the station B profile was not resolved. However, the difference in the measured w_{rms} profiles at $z = 2h_m$ between stations A and B is just evident (fig.6d). These data suggest that elements even $5h_m$ upstream can make crucial contributions to the turbulence statistics, if they are sufficiently tall with respect to h_m.

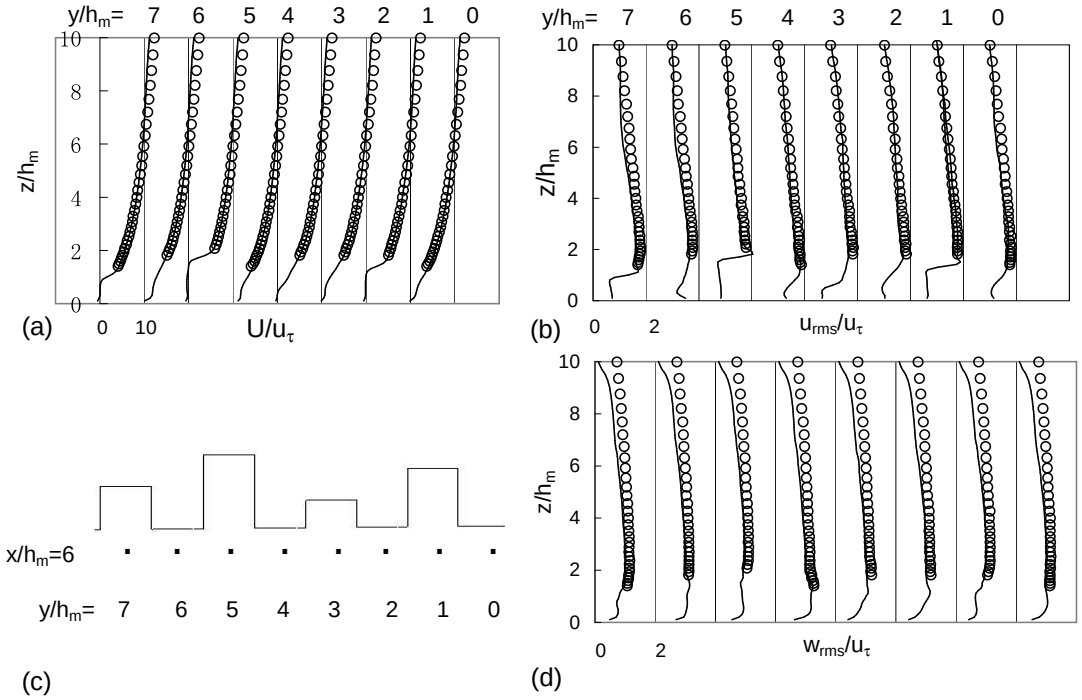

Figure 5. Mean and r.m.s velocity profiles behind row three (i.e. on the chain-dotted line in fig.2). Symbols, measurements; lines, LES.

We conclude that the present LES computation provides data in reasonable agreement with laboratory experiment, particularly in the near-surface region. This is entirely consistent with the conclusion of XC for uniform surfaces, which included comparisons with (LDA) data obtained below $z = h$ as well as with DNS results, and thus provides confidence in the adequacy of the LES data within the canopy region of the present random surface.

3.2. The overall canopy flow and surface pressure.

Figure 7 shows mean velocity vectors (U, V) on the horizontal plane $z = 0.5h_m$ and (V, W) on the vertical plane $x = 5.6h_m$ (immediately behind row 3). These data are averages over the four repeating units. The details within the canopy are complicated and depend greatly on the arrangement and the height of the blocks. For example, on the right side (facing downstream) of the 10 mm block in row 1, near station A there is a large separation bubble, whereas on the left side there is no bubble because on that side the 13.6 mm block and 10mm block form a relatively narrow channel, giving a strong negative pressure gradient in the streamwise direction - suppressing the reverse flow. This contrasts with the flow around the next 10 mm block just downstream and on the left, where there are similar separated zones on both sides. In the wake of this block, however, there is clearly a

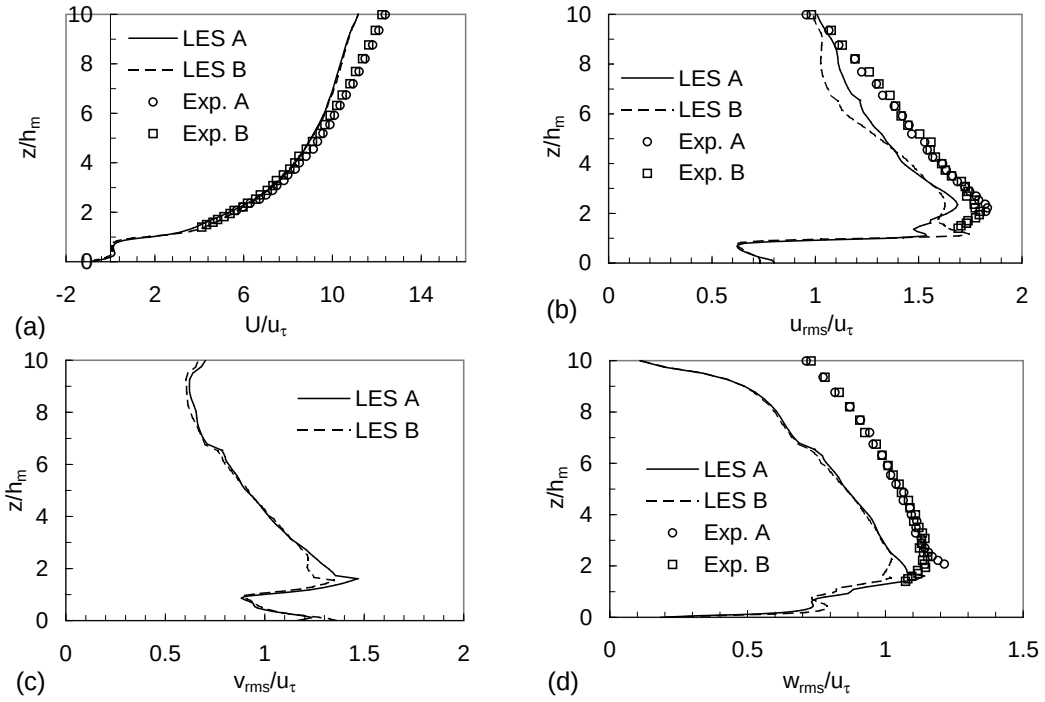

Figure 6. A comparison of streamwise mean velocity and velocity r.m.s. profiles between stations A and B (see Figure 7).

strong asymmetry, presumably caused by the spanwise pressure gradient generated by the dissimilar height blocks on either side. On the vertical plane, a common phenomenon is that in the gaps between rows the flow is downward; consequently a clockwise circulation (looking upstream) is formed on the right side of the 17.2mm block (anti-clockwise on the left-hand side), as illustrated by the large arrows in fig.7b. This is the reverse of what would occur for an isolated single block, where the cross-stream circulations have the same sense as those in a trailing vortex system behind, for example, a delta-wing. Its cause is the strong down-flow downstream of the gap, e.g. on the right of the 17.2mm block (facing downstream), generated by the 13.6 mm block just downstream. The result emphasises that even the qualitative behaviour of the flow around a particular building surrounded by others may be very different from what would occur if the building were more remote, suggesting that extreme caution is necessary in extrapolating what might be known about the latter situation.

Figure 8 shows corresponding contours of turbulent kinetic energy (TKE) on the $z = 0.5h_m$ plane, which reveal some interesting features. It would not be intuitively obvious, for example, that the regions with the highest levels of TKE would not only include the regions to the sides of the tallest (17.2 mm) block but also downstream of the 13.6 mm block in the first row; maximum levels in these two regions are within a percent of each

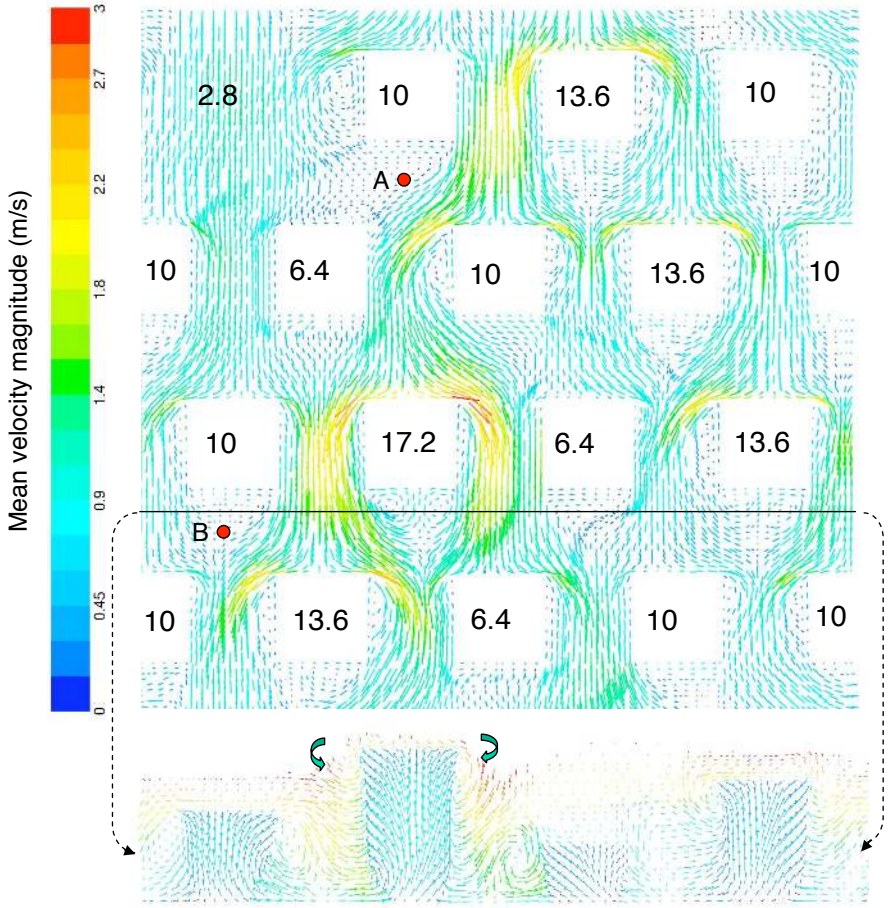

Figure 7. Mean velocity vectors (U,V) at z = 0.5 h_m (top, flow is from top to bottom) and (V,W) at x = 5.6 h_m (bottom, looking upstream). Note the location of the two solid red circles, labelled A and B, which are discussed in the text.

other and are clearly significantly higher (by some 30%) than in the region downstream of the 17.2 mm block. Note too that the high TKE around the sides of the tallest block is greatest in the region behind the tallest block just upstream (10 mm cf. 6.4 mm). It is quite clear from both these figures that the flow and turbulence fields around the average height (10 mm) blocks depend strongly on the height of the surrounding blocks, particularly those just upstream. Similar conclusions result from inspections of the data on different z-planes, but for planes above $z = h_m$ there are some noteworthy differences. These are illustrated by figure 9, which shows TKE contours at four heights. It is clear that the tallest building dominates in setting the largest values of TKE. Alternative arrangements of the blocks (e.g. placing the lowest block in one of the six positions immediately adjacent to the tallest block, rather than two rows away) would undoubtedly lead to yet another

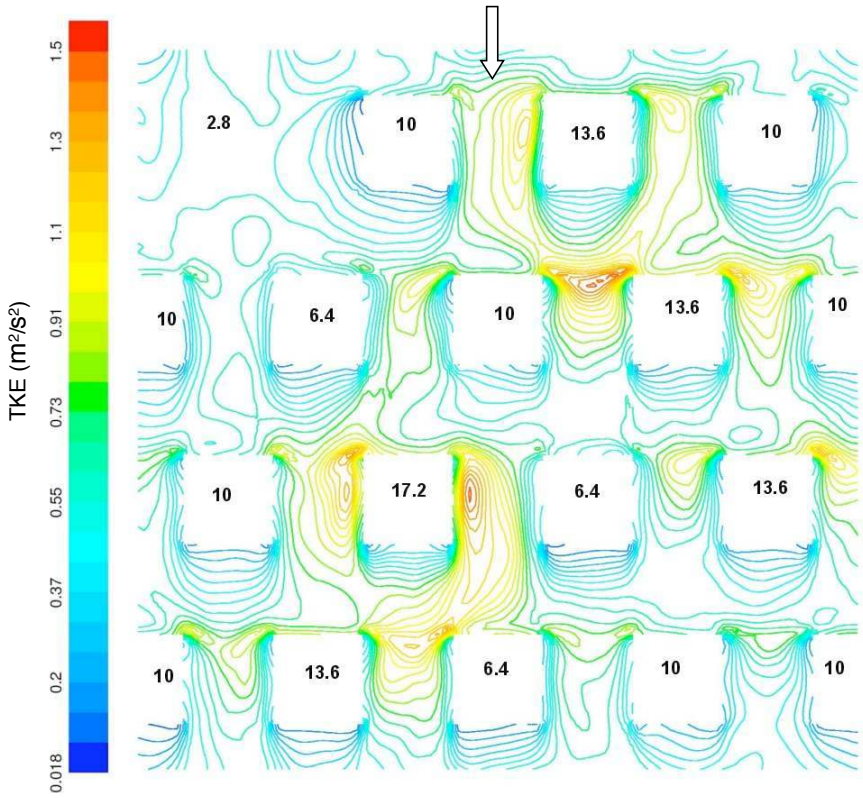

Figure 8. TKE contours at z = 0.5 h_m in a repeating unit.

set of flow patterns, but probably with similar differences in the flows around individual blocks.

The different flows around each block are linked of course with different pressure fields on their surfaces. Figure 10 presents the normalised profiles of the drag force on each of the 16 obstacles in a repeating unit. The tallest block (17.2 mm) exerts much more drag than the others. In fact, it is alone responsible for 22.4% of the total drag - far in excess of its proportionate frontal area (10.8%) within the array. The five tallest blocks (the 17.2 mm and the four 13.6 mm ones) are together responsible for two-thirds (65.3%) of the total drag, although their frontal area is only 44.8% of the total. This is summarised by the Pie chart included in fig. 10a, which shows the percentage contribution to the total surface drag provided by the three groups of blocks. The shapes of the drag profiles (fig. 10a) are in general similar for many of the tallest buildings (17.2 mm, 13.6 mm, 10.0 mm) except when they are in the vicinity of a taller building. The profile shapes for the shortest buildings (6.4mm and 2.8mm) are very different, as emphasised by fig.10b, where the pressure difference normalised by the mean pressure difference across each block is plotted with height normalised by the corresponding block height. These buildings, however, do

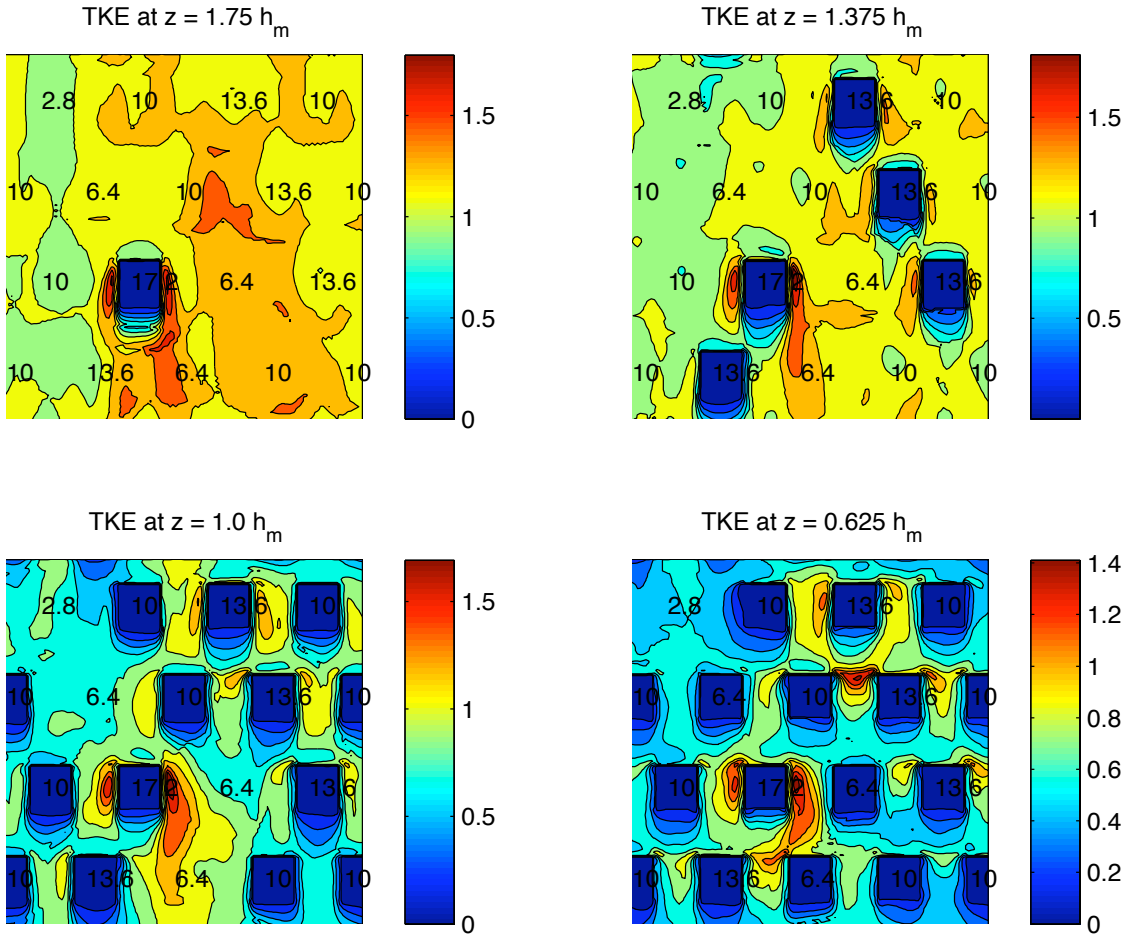

Figure 9. TKE contours at $z/h_m = 0.625, 1.0, 1.375$ & 1.75 in a repeating unit. Flow is from top to bottom.

not exert much drag as is clear from fig.10a. The fact that the tallest block exerts a disproportionate amount of drag is consistent with some recent experimental findings. Hayden *et al.* (2007), for example, studied the uniform (10 mm) cube array of CC, but varied the height of one of the cubes; they found that a mere 15% increase in this height led to a 45% increase in its drag coefficient. These results are not surprising, given the fact that the majority of the drag force on each block arises from its upper portion, as is clear from fig.10a, and that the velocities increase with height rapidly through the region surrounding the top of the canopy.

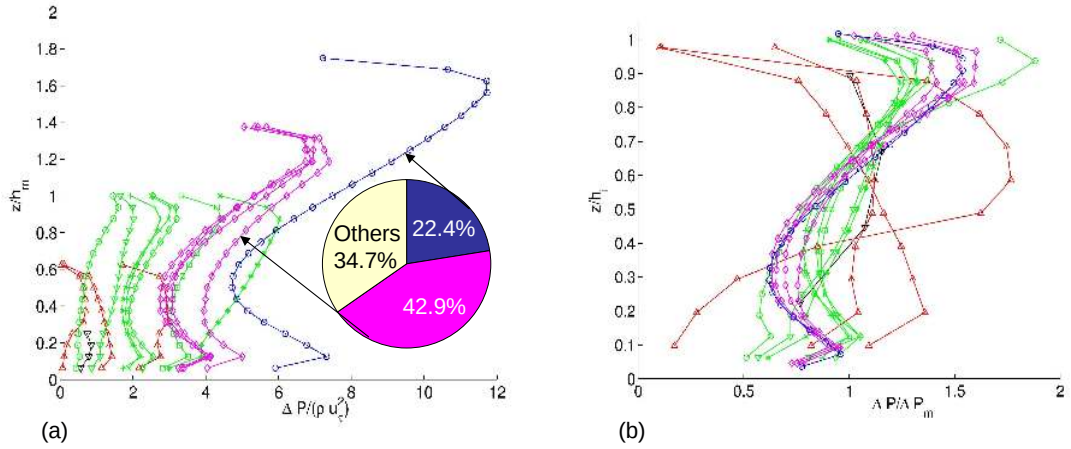

Figure 10. Normalised profiles of the drag force on each of the 16 obstacles in a repeating unit of the random array. (a): the laterally integrated pressure difference between the front and back faces of the cube, normalised by ρu_τ^2. (b): pressure difference normalised by the mean pressure difference on each block, with z normalised by the individual block height.

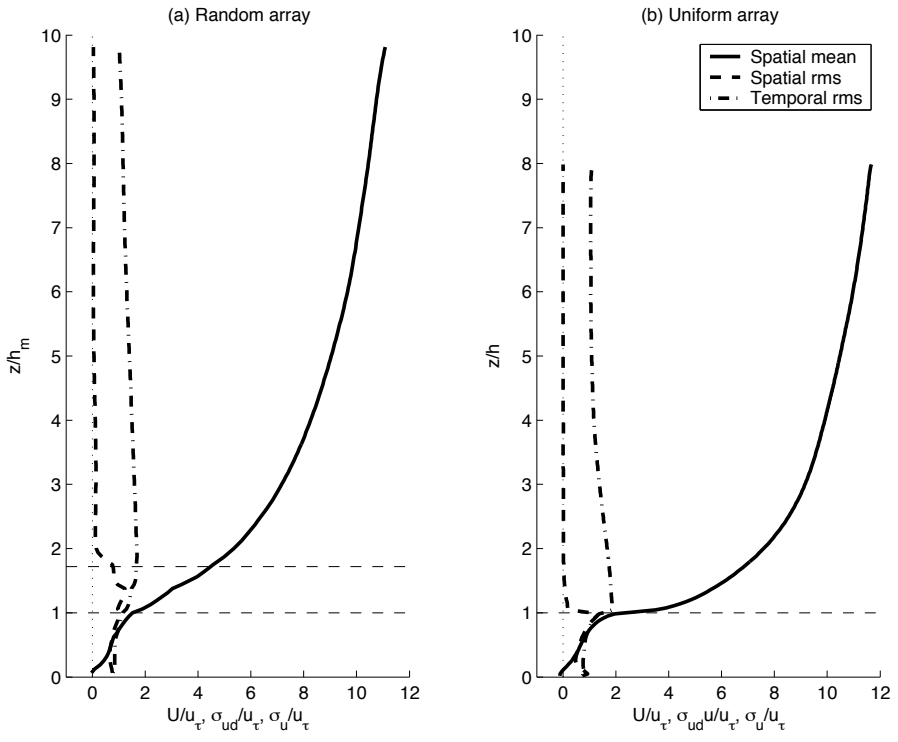

Figure 11. Profiles of spatially-averaged axial mean velocity (U), fluctuating velocity ($u_{rms} = \sigma_u$), and r.m.s. dispersive stress ($< \tilde{u} >^{1/2} = \sigma_{ud}$), normalised by u_τ. The dashed lines indicate the average height of the blocks and, in (a), the height of the tallest block.

3.3. Comparison between spatially averaged statistics over random and regular arrays

It is instructive to compare how the flow over the random array compares with that over the uniform array. Figure 11 shows profiles of spatially-averaged axial mean velocity, r.m.s. fluctuating velocity and the r.m.s of the dispersive stress ($< \tilde{u}^2 >^{1/2}$, where $\tilde{u}$ denotes the spatial variation from the time-mean flow as resolved by the LES) for the random array (a) and the uniform array (b) of Coceal *et al.* (2007b). Note that the usual partition of stresses into time-averaged and spatially-averaged (dispersive) components, which is exact in DNS, is less clear when, as in LES, sub-grid models are used. Strictly, there are *four* contributions (which include the sub-grid parts of both time and space averaging processes), but in the present work we have ignored all sub-grid effects so that the data shown in Figs. 11, 13 & 14 should be viewed as *estimates* of the relative contributions – being calculated as if the unresolved sub-grid stresses are zero. Above the height corresponding to that of the uniform canopy, the mean velocities are significantly smaller over the random array since this array exerts more drag and has a larger roughness length. Within the canopy region, however, the velocities are very similar to those in the random array. There is a noticeable inflection in the velocity profile roughly at the canopy top in the uniform array. This is associated with a strong shear layer at the cube tops. In contrast, the profile over the random array has a much weaker inflection, at a height somewhat above the mean building height of 10 mm. Likewise, similar behaviour of the fluctuating components are apparent in the two cases. So, for example, in the canopy region the spatial and temporal r.m.s. values are in both cases of the same order as the mean velocity, and above the canopy the dispersive stress, unlike the usual (temporal) stress, rapidly becomes very small. The fact that within the canopy both the spatial averages and the spatial standard deviation of spatial variations from this average are very similar for both arrays is somewhat surprising. It implies that, at least in an integral sense, the flow below the mean building height in the random array is just as spatially inhomogeneous as that within the regular array, but no more.

Figure 12 compares normalised profiles of spatially-averaged streamwise, spanwise and vertical turbulent stresses and the TKE (i.e. one half of their sum) for the random and uniform arrays. Again, roughly similar values between the two cases were found below the mean building height. The peaks in streamwise turbulence intensity and TKE for the uniform array are stronger than those for the random array, because a stronger shear layer develops over the cubes of uniform height, as noted earlier; the locations of these peaks are in that case near the cube tops. In the random array, the peaks are less strong, but still quite pronounced. Interestingly, they occur at the height of the tallest building, not at the mean building height, even though these are the spatially averaged profiles. This suggests yet another way in which the effects of tall buildings dominate - as well as exerting proportionately more drag, they produce a lot more TKE, as suggested too by the TKE contours in fig. 9.

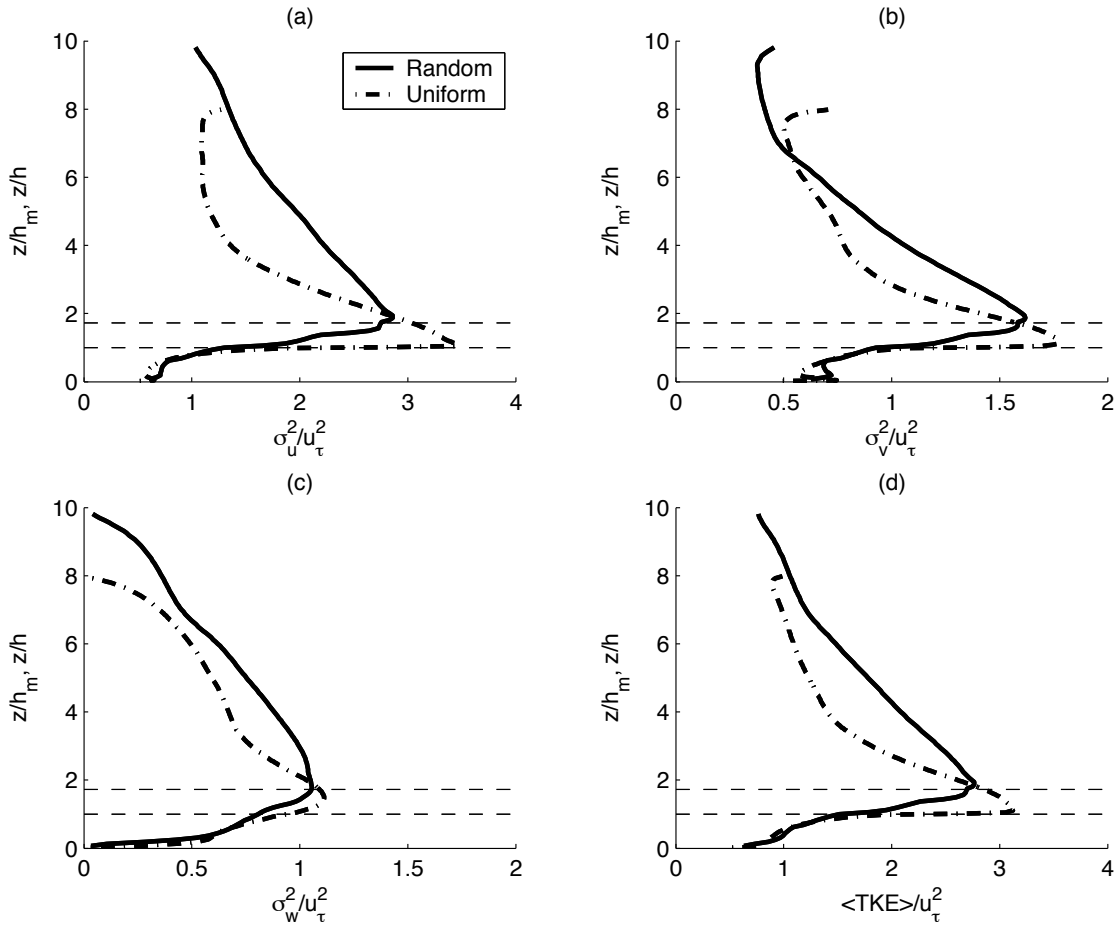

Figure 12. Profiles of spatially averaged streamwise, spanwise and vertical turbulent stresses and TKE.

Some features of the stresses near the top and bottom boundaries are also worth mentioning. Fig.12b shows a small rise in the spanwise stress component as the upper (symmetry) boundary is approached. Shaw & Schumann (1992) have pointed out that the kind of boundary condition used here can be interpreted as a strong inversion; like turbulence near a wall, one expects the energetic larger-scale eddies to 'splat' as they approach the boundary, with energy being transferred into the directions parallel to the boundary from the component normal to it. The normal component (Fig.12c) certainly falls to zero as it should and it is probably this process which leads to the noticeable rise in spanwise stress; this 'splatting' behaviour is also apparent in the DNS of Coceal *et al.*(2006). A similar process occurs near the bottom boundary within the canopy, except that there all stresses must fall to zero at the wall. But the boundary layer at the surface is very thin and, although the DNS computations shown in XC (from Coceal *et al.*, 2006)

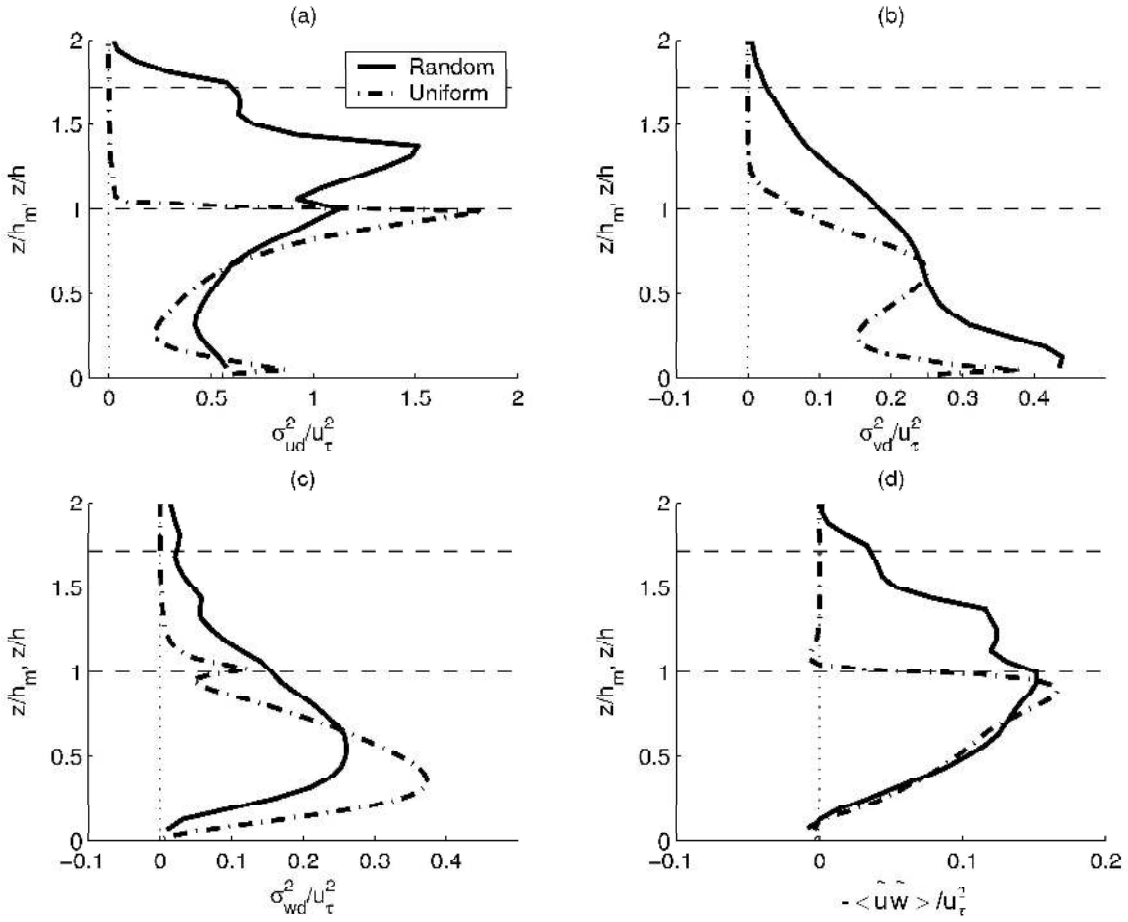

Figure 13. Profiles of dispersive stresses within and immediately above the canopy regions.

show not only the 'splatting' peak in spanwise stress but the subsequent fall to zero at the wall, the present LES grid is too coarse to capture the latter.

Figure 13 plots profiles of the dispersive stresses, normalised by u_τ^2, within and immediately above the canopy regions for the random and uniform arrays. (Recall our notation for these stresses – $< \tilde{u}_i \tilde{u}_j >$, with $i = j = 1$ for the axial component, etc., and, for example, $\sigma_{ud}^2 =< \tilde{u}_1 \tilde{u}_1 >$.) Profiles of the shear component of dispersive stress are very similar below $z = h_m$. Differences are apparent in the case of the normal components, perhaps resulting from differences in the irrotational contributions because of the much larger variations in the mean flow within the random array. Above the (average) height of the random array the dispersive stresses fall towards zero much more slowly than in the uniform array, no doubt because there remain significant inhomogeneities in building heights above $z = h_m$.

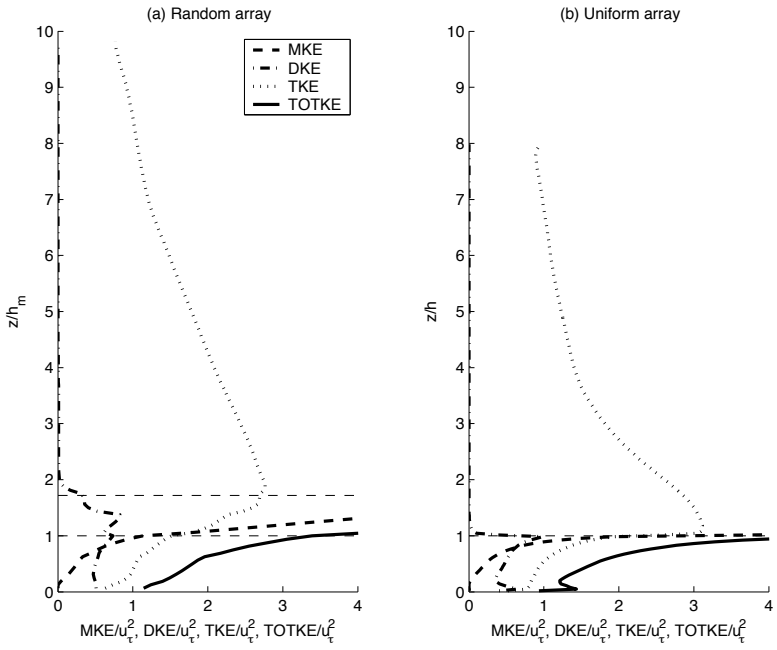

Figure 14. Profiles of the three components of kinetic energy, namely mean K.E. (MKE = $0.5< \bar{u}_i >^2$), dispersive K.E. (DKE=$0.5< \tilde{u}_i\tilde{u}_i >$) and TKE ($0.5< \overline{u_i'u_i'} >$).

Figure 14 shows profiles of the three components of kinetic energy, namely mean kinetic energy (MKE = $0.5< \bar{u}_i >^2$), dispersive kinetic energy (DKE=$0.5< \tilde{u}_i\tilde{u}_i >$) and the usual turbulence energy (TKE=$0.5< \overline{u_i'u_i'} >$), all normalised by u_τ^2. TOTKE denotes the sum of the resolved mean, turbulence and dispersive kinetic energies, respectively. MKE dominates above the canopy, but rapidly becomes a negligible fraction of the total kinetic energy within the canopy, while the fraction of DKE and TKE both increase. DKE is nearly uniform through most of the canopy depth for both arrays (fig.14). The fractions of MKE, DKE and TKE for the two arrays are very similar below $z = h_m$; energy is partitioned roughly in the same proportions. Above the canopy, the TKE fraction over the random array is roughly twice as large as that over the regular array - again, an indication of the significantly rougher surface conditions caused by the non-uniform block heights.

3.4. Generality of turbulence statistics within the canopy region

Coceal *et al.* (2007a) attempted to identify three flow regimes in the (staggered) uniform array of cubes, which were described as a constricted region (R1), a front-recirculation region (R2) and a building wake region (R3) (see Figure 2). Each of these has the same horizontal extent as that of an individual cube. More, but smaller, regions could of course

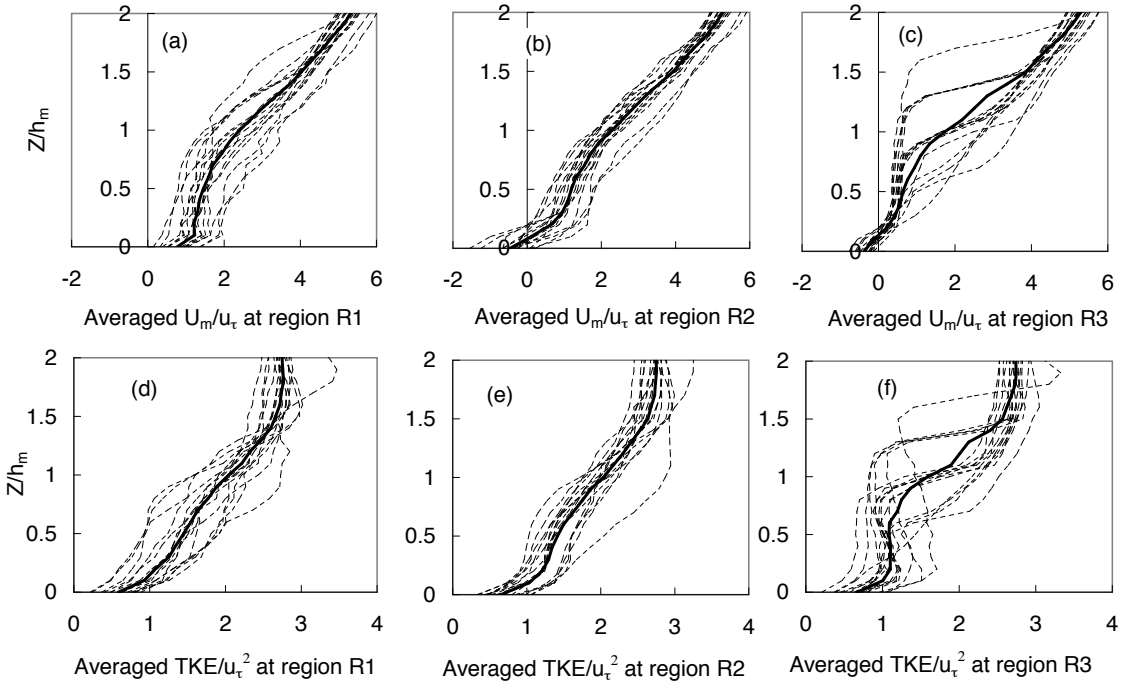

Figure 15. Locally spatially averaged U_m and TKE profiles over the region in a repeating unit. Solid lines are the ensemble averaged profiles over the 16 corresponding regions.

have been chosen, but the hope was that these three were small enough to allow a general characterisation of the flow within each, without being so large that quite independent flow characteristics could be identified within one or more of them. In the repeating unit of the random array, there are sixteen of each of these regions but, not surprisingly, the present results show that the flow statistics (e.g. U_m, TKE) within one region differ significantly from those in another region having the same identity (R1, R2 or R3), because of the different block topology surrounding them. Even if the turbulence statistics were averaged horizontally over the whole local region the scatter between the sixteen regions is very evident, as shown in Figure 15. Particularly for the R1 and R3 regions (figs.15a & c), the flow is clearly strongly influenced by the local blocks. For R2 the rather better overall convergence of the sixteen profiles might indicate that in this region the flow is generally less influenced by the local blocks, which is perhaps not unexpected, given that the nearest block is always downstream of this region.

The convergence of the sixteen U_m profiles is noticeably better than that in fig. 15c if the vertical coordinate is normalised by the block height immediately in front of the region. This implies that the mean flow in this region is most strongly influenced by the block immediately upstream. The sixteen TKE profiles are also then more similar in form than those in fig.15f. When, in addition, the TKE is normalised by its value integrated from $z/h_i = 0$ to 1 even better convergence of the sixteen profiles was found (not shown),

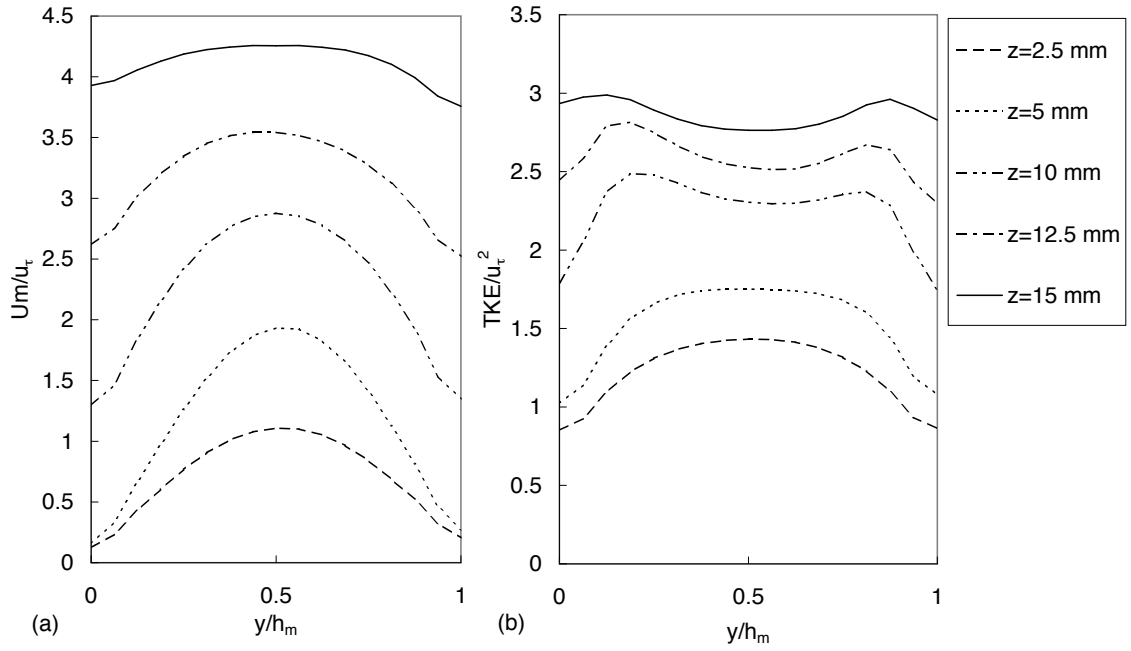

Figure 16. Averaged U_m and TKE over sixteen R1 regions at the spanwise centre line in a repeating unit.

but the magnitude of the TKE was more sensitive (than that of the mean velocity) both to the height of the block in front of the region and to the upstream conditions.

It is also of note that U_m and the TKE at the spanwise centre line in one R1 region could differ dramatically from those in another R1 region. The heights of the blocks on both sides of the R1 region highly influence the form and magnitude of the spanwise profiles of U_m and TKE. Figure 16 shows spanwise U_m and TKE profiles at five heights, averaged over the sixteen R1 regions on the spanwise centre line; these have an approximately similar form to those of the uniform array of cubes (Coceal *et al.*, 2007a).

Overall, the results discussed above suggest that it is not possible to identify individually just a few typical regimes for the random array of staggered blocks, as Coceal *et al.* (2007a) did for the uniform array. So a natural question is to ask whether local conditions within a single region (which we continue to define by a horizontal area equal to the cube plan area) can be determined largely by knowledge of the heights of the nearest blocks. To answer this, we investigate the relation between the mean streamwise velocity or TKE (e.g. at the centre of region R1 at $z = 0.25h_m$) and the local topology, i.e. the block heights. Assume for the moment that the mean streamwise velocity and the TKE at the marked station ($z = 0.25h_m$) between blocks 1 and 2 (see Figure 17) follow, respectively,

$$\frac{U_m}{u_\tau} = \frac{1}{h_m}(c_1h_1 + c_2h_2 + c_3h_3 + ... + c_8h_8) + const_1, \tag{5}$$

and

$$\frac{TKE}{u_\tau^2} = \frac{1}{h_m}(d_1h_1 + d_2h_2 + d_3h_3 + ... + d_8h_8) + const_2, \quad (6)$$

where $h_1, h_2, h_3, ...h_8$ are the heights of the nearest eight blocks, as indicated in Figure 17, and $c_1, c_2, c_3, ...c_8, const_1$, $d_1, d_2, d_3, ...d_8$ and $const_2$ are coefficients to be obtained by using a least square (LS) regression.

A part of one repeating unit was processed to obtain the coefficients, and the remaining part of the unit was then examined to see whether (5) and (6) would yield reasonable values of the two parameters. Arbitrarily, three rows of blocks (12 points) were used for the regression and the remaining one row (4 points) for the validation of the prediction obtained by using the resulting nine fitted coefficients. As a typical test case, rows 2, 3 and 4 in one repeating unit were processed and row 1 was used for validation. Figure 17 shows the fitted (rows 2, 3 & 4) and predicted (row 1) U_m and TKE against the original LES data. The same coefficients were also used to predict the U_m and TKE for the uniform array of staggered cubes, i.e. the triangles in fig. 17. Table I shows the coefficients (5) and (6) obtained from the fitting process.

Table I. Comparison of similarity coefficients in the surface layer

c_1	c_2	c_3	c_4	c_5	c_6	c_7	c_8	$const_1$
-0.054	0.798	0.798	0.080	0.017	0.080	-0.044	-0.044	0.035
d_1	d_2	d_3	d_4	d_5	d_6	d_7	d_8	$const_2$
-0.403	0.504	0.504	0.143	0.265	0.143	-0.037	-0.037	0.317

Figure 17 suggests that the mean flow and the TKE are indeed strongly influenced by the local geometry of the canopy but the scatter might suggest that the flow is also influenced by the more remote flow conditions, as discussed in §3.1. It is speculated that such a method could also be applied for region R2 and R3, but it is not clear whether the process would allow useful information to be gleaned for real urban situations. Whilst this could be an interesting avenue for further work, the results discussed above suggest that complete generalisation of the approach of Coceal *et al.* (2007) – identifying a usefully small number of 'typical' flow regions within any canopy – may not be very helpful, or even possible.

3.5. Further turbulence characterisation

An additional indicator often used to help understand the character of a turbulent flow is the anisotropy tensor defined by

$$b_{ij} = \overline{u_i u_j}/\overline{u_k u_k} - \delta/3$$

and its second and third invariants, $II = -b_{i,j}b_{ji}$ and $III = b_{ij}b_{jk}b_{ki}$, which were originally defined by Lumley (1978). Figure 18a shows an anisotropy invariant map (AIM), in which

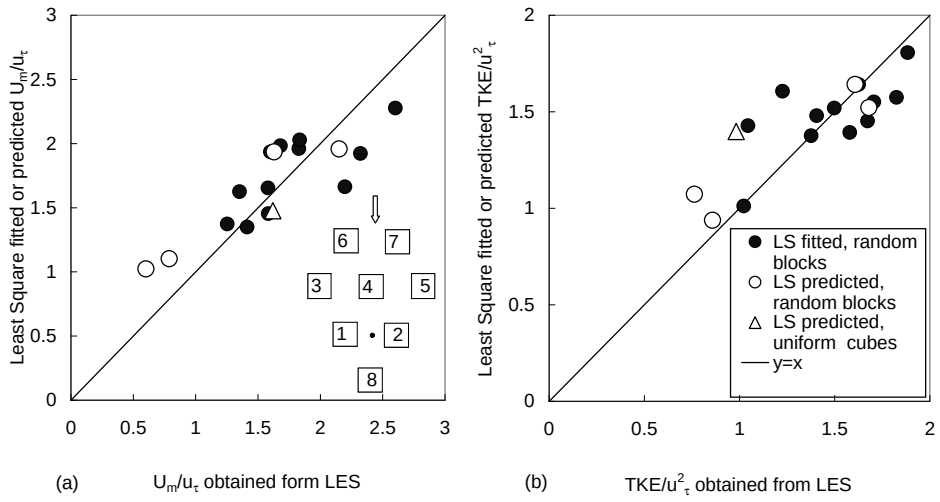

Figure 17. Fitted and predicted U_m (a) and TKE (b) at z=0.25h_m in the gap (region R1). Solid symbols, fitted (for rows 2, 3 & 4); open symbols: predicted (row 1 of random array and uniform array). Triangles: predicted, for uniform array.

-II indicates the degree of anisotropy (it would be zero for genuinely isotropic turbulence) and III represents the nature of the anisotropy. All possible states of turbulence occur in the so called Lumley triangle, of which only some segments are visible in Figure 18a. The turbulence along the upper straight line is in the 2-D state. Choi & Lumley (2001) identified that turbulence on the left-curved boundary is 'pancake'-turbulence with one component of the turbulent kinetic energy being much smaller than the other two; on the right-curved boundary is 'cigar-shaped' turbulence with one component of the turbulent kinetic energy being significantly greater than the other two. Data are shown (in the canopy region only) for the three locations at the centre of each of the regions previously discussed; so, for example, the P1 data refer to points along the vertical line through the centre of R1 (fig.2). Each data point is an average across all 64 possible positions within the entire computational domain.

All the data fall into a very small area in the vicinity of the origin, which is more or less the same as found for flow over the uniform array by Castro *et al.* (2006), but differs significantly from near-surface data in smooth-wall boundary layers or within the two-dimensional canopy region formed by transverse bars, studied by Smalley (2002), which both have rather larger -II/III combinations. This indicates that the turbulence within and immediately above staggered arrays is more isotropic than in the corresponding region of a smooth-wall boundary layers or a two-dimensional canopy. Most of the curves within the canopy layer are nearly parallel and are closer to the right boundary than to the left boundary of the Lumley triangle, which indicates that one component of the turbulent kinetic energy is generally rather larger than the other two within the canopy layer. Another major feature is that all the roughness sublayer data above the CR (not shown in fig.19 for clarity) collapse near the point (-II=0.038, III=0.001). This is very

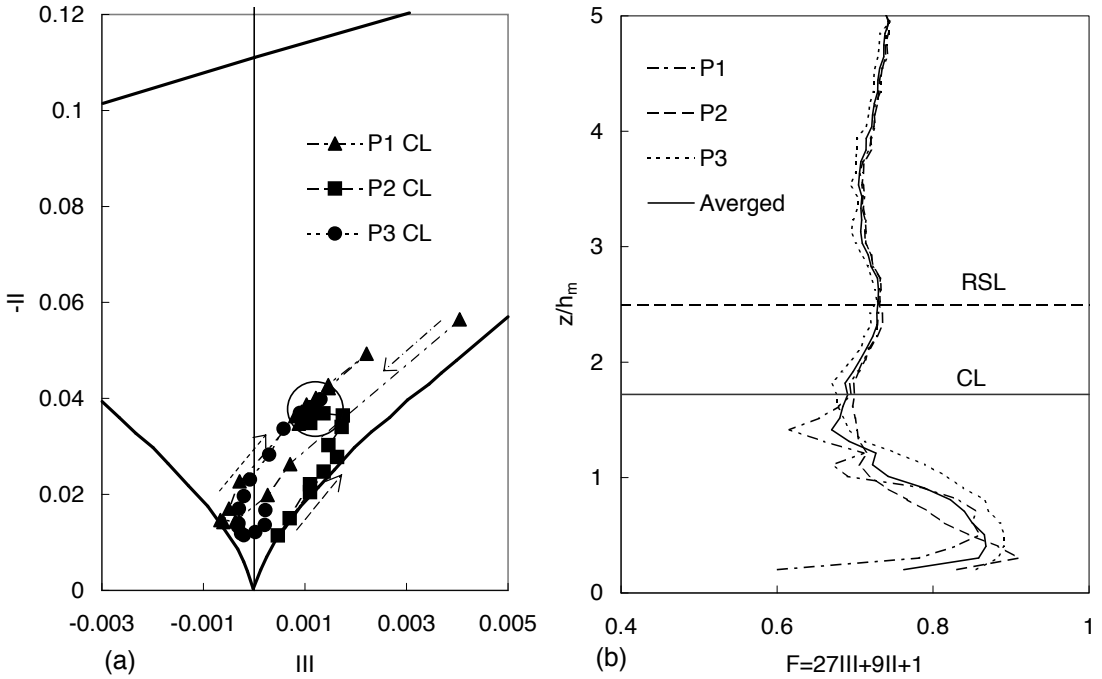

Figure 18. (a), AIM for locations P1, P2 and P3 within the canopy layer (CR). P1, P2 and P3, centre of R1, R2 and R3 respectively (see Figure 2) . Arrows indicate increasing z. Heavy solid lines refer to segments of the Lumley triangle and data within the RSL lie entirely within the region identified by the circle centred near $-II = 0.038, III = 0.001$. (b), anisotropy function $F = 27III + 9II + 1$ for P1, P2 and P3 in the surface layer. The solid and dash lines respectively refer to the top of the highest block and the top of the roughness sublayer (RSL).

different from the behaviour over the uniform array, where the experimental data of Castro *et al.* (2006) indicate that, for example, along P1 III ranges between zero and about 0.0035 in the RSL. So it seems that in the region just above the random array the turbulence structure is much more uniform.

The function $F = 27III + 9II + 1$ (Lumley, 1978) provides a single parameter for distinguishing how remote is the turbulence from being fully isotropic ($F = 1$) or in a 2-D state ($F = 0$). Figure 18b shows the anisotropy function for P1, P2 and P3 within and immediately above the canopy. The solid line is the mean of the P1, P2 and P3 profiles. Again, each profile was obtained by averaging profiles at all sixty-four of the available stations. Note that in a smooth-wall boundary layer F remains below about 0.6 for $z/\delta < 0.5$ (see, for example, Erm & Joubert, 1991). Within the roughness sublayer, above the canopy layer, the differences between the profiles at P1, P2 and P3 are hardly discernible, which again differs from the uniform array results, where F varied 0.6 and 0.8 (Castro *et al.*, 2006). In the canopy region, however, the variations are larger and are very similar to those found for the uniform array. The minimum F occurs at P1 just below

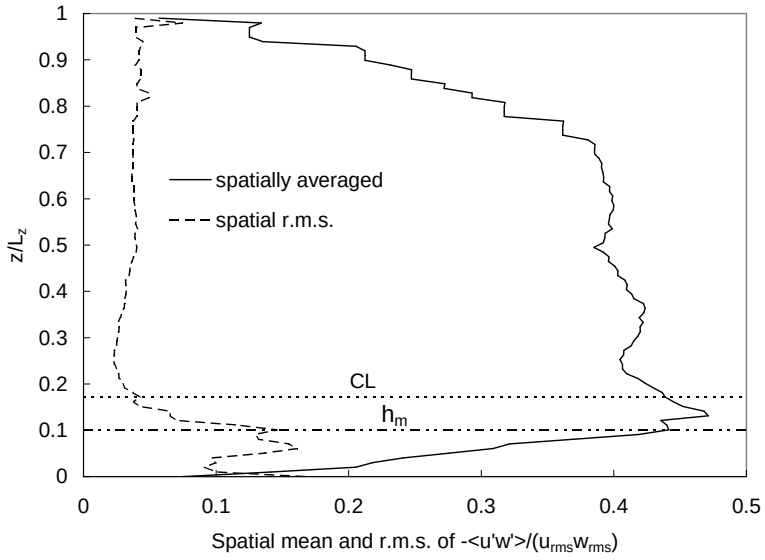

Figure 19. Spatially averaged mean and the spatial r.m.s of the correlation coefficient $r_{uw} =< \overline{u'w'} > /(u_{rms}w_{rms})$.

the top of the canopy layer and is about 0.6 – a little greater than for the uniform array. This is because the shear layer around $z = h_m$ is wider and weaker than in the uniform array, as noted earlier. The maximum F occurs between $z = 0.3h_m$ and $z = 0.5h_m$ and is somewhat larger at P2 and P3 than at P1.

Finally, defining $r_{uw} = - < \overline{u'w'} > /(u_{rms}w_{rms})$ as the shear stress correlation coefficient, as usual, Figure 19 shows the spatially averaged mean and the r.m.s. of r_{uw} for flow over the random array. In the region immediately above the canopy the correlation coefficient is approximately 0.4, which is close to the experimental value (0.38-0.39) found by CC. However, it is significantly higher than the correlation coefficient in the surface layer over a uniform array (as also previously noted by CC) – by some 9% – which indicates an increased 'turbulence efficiency' in the generation of shear stress. Within the canopy the correlation coefficient increases roughly linearly from about 0.1 to 0.47 at $z = 1.4h_m$, suggesting an increasing importance of turbulence production.

4. Conclusions

There are a number of major conclusions arising from the data presented and discussed above. Firstly, it has been shown that the flow within the canopy region generated by random height blocks (buildings, in the urban context) is significantly more complex than it is in the case of uniform height blocks. Although spatially averaged means and spatial standard deviations from these means are quite similar in the two kinds of arrays, there

are many features of the flow over the random roughness which are rather different from those in the flow over uniform roughness. It would not always be possible to deduce these features on the basis of what is known about flow over isolated elements. Secondly, the tallest elements have been found to generate disproportionate contributions to the surface drag and to, for example, turbulence kinetic energy above the average element height. Nonetheless, in the region just above the random array, turbulence structure is significantly more uniform than it is above a uniform array. Thirdly, it would appear to be difficult to generalise the approach of Coceal *et al.*(2007) by identifying a relatively small number of basic flow regions, whose characteristics could be estimated on the basis of the topology of the surrounding blocks, and thence characterise the whole domain. The results suggest that the canopy flow local to any individual block can be significantly influenced by relatively remote blocks. It is perhaps unlikely that the approach proposed here could be helpfully exploited for real, urban situations. This highlights the importance of undertaking simulations of entire domains, either by laboratory experiment or numerical computation, if useful information is to be obtained for specific, full-scale situations. Finally, it is emphasised that numerical computations *can* provide such information; our results show reasonable agreement with experimental data, for quantities which can actually be measured. In view of the inherent unsteadiness in these flows we believe that Large Eddy Simulation techniques provide an appropriate approach.

Acknowledgment: This project is supported by NERC under the Weather Directorate of NCAS, the National Centre for Atmospheric Science (Grant No. DST/26/39). The authors are grateful to their colleague Dr Glyn Thomas for numerous helpful discussions and to the referees for some illuminating comments.

References

Castro I.P., Cheng H. and Reynolds R. (2006) Turbulence over urban-type roughness:decutions from with tunnel measurements, *Bound.-layer Meteoro.*, **118**, 109-131.

Choi K.-S. and Lumley J.L. (2001) The return to isotropy of homogeneous turbulence, *J. Fluid Mech.* **436**, 59-84.

Cheng H. and Castro I.P. (2002) Near wall flow over urban-like roughness, *Boundary-Layer Meteorol.* **104**, 229-259.

Coceal O., Thomas T.G., Castro I.P. and Belcher S.E. (2006) Mean flow and turbulence statistics over groups of urban-like cubical obstacles, *Boundary Layer Meteorol.*, **121**, 491-519.

Choudhury D, Kim S.E., Makarov B.P., Carey C. (2004) Improved numerical methods for CFD solutions on unstructured meshes, *ERCOFTAC bulletin* **62**, 13–18.

Coceal O., Thomas T.G. and Belcher S.E. (2007a) Spatial variablity of flow statistics within regular building arrays, *Boundary Layer Meteorol.*, in press.

Coceal O., Dobre, A., Thomas T.G. and Belcher S.E. (2007b) Structure of turbulent flow over regular arrays of cubical roughness, *J. Fluid Mech.*, **589**, 375-409.

Erm L.P. and Joubert P.N. (1991), Low-Reynolds-number turbulent boundary layers, *J. Fluid Mech.* **230**, 1-44.

Hanna S.R., Tehranian S., Carissimo B., Macdonald R.W. & Lohner R. (2002) Comparisons of model simulations with observations of mean flow and turbulence within simple obstacle arrays, *Atmos. Environ.* **36**, 5067-5079.

Hayden P., Mapurisa T. & Robins A.G. (2007) Spanwise variation of drag on roughness elements in a nominally two-dimensional boundary layer. Paper presented at PHYSMOD2007, Univ. of Orleans, France, August 2007.

Kanda M. (2006) Large-Eddy Simulations of the effects of surface geometry of building arrays on turbulent organised structures. *Boundary Layer Meteorol.* **118**. 151-168

Kanda M., Moriwaki R. & Kasamatsu F. (2004) Large-eddy simulation of turbulent organized structures within and above explicitly resolved cube arrays. *Boundary-Layer Meteorol.* **112**, 343-368.

Kastner-Kline P. & Rotach M.W. (2004) Mean flow and turbulence characteristics in an urban roughness sublayer. *Boundary layer meteorol.* **111**, 55-84.

Lumley J.L. (1978) Computational modelling of turbulent flows, *Adv. Appl. Mech.* **18**, 123-126.

Meinders E.R. & Hanjalić K.(1999) Vortex structure and heat transfer in turbulent flow over a wall-mounted matrix of cubes, *Int. J. Heat Fluid Flow* **20**, 255-267.

Moeng C.-H. (1984) A Large-Eddy Simulation Model for the Study of Planetary Boundary Layer Turbulence, *J. Atmos. Sci.* **41**, 2052–2062.

Moreau S., Mendonca F., Qazi O., Prosser D., Laurence D. (2004) Influence of turbulence modelling on airfoil unsteady simulations of broadband noise sources, *AIAA J.* 2005-2916.

Peric M. (2004) Flow simulation using control volume of arbitrary polyhedral shape, *ERCOFTAC bulletin* **62**, 25–29.

Shaw, R. H. & Schumann, U. (1992) Large Eddy Simulation of Turbulent Flow above and within a Forest, *Boundary-Layer Meteorol.* **61**, 47–64.

Smalley R.J., Leonardi S., Antonia R.A., Djenidi L. & P. Orlandi (2002) Reynolds stress anisotropy of turbulent rough wall layers, *Exp. Fluids* **33**, 31-37.

Stoesser T., Mathey F., Frohlich J. and Rodi W. (2003) LES of flow over multiple cubes. ERCOFTAC Bulletin No. 56.

Xie Z.-T., Castro I.P. (2006) LES and RANS for turbulent flow over arrays of wall-mounted cubes, *Flow,Turbulence and Combustion*, **76** (3), 291-312.

Xie Z.-T., Castro I.P. (2008) Efficient generation of inflow conditions for Large Eddy Simulation of street-scale flows, *Flow,Turbulence and Combustion*, in press.

Yoshizawa, A. (1986) Statistical theory for compressible turbulent shear flows, with the application to subgrid scale modelling, *Phys. Fluids* **29**, 2152– 2164.